

Large Magnetocaloric Effect in the Kagome Ferromagnet $\text{Li}_9\text{Cr}_3(\text{P}_2\text{O}_7)_3(\text{PO}_4)_2$

Akshata Magar,¹ Somesh K,¹ Vikram Singh¹, J.J. Abraham^{2,3}, Y. Senyk,² A. Alfonsov,²
B. Büchner,^{2,4} V. Kataev², A.A. Tsirlin⁵, and R. Nath^{1,*}


¹*School of Physics, Indian Institute of Science Education and Research Thiruvananthapuram, Kerala 695551, India*

²*Leibniz IFW Dresden, Dresden D-01069, Germany*

³*Institute for Solid State and Materials Physics, TU Dresden, Dresden 01069, Germany*

⁴*Institute for Solid State and Materials Physics and Würzburg-Dresden Cluster of Excellence ct.qmat, TU Dresden, Dresden D-01062, Germany*

⁵*Felix Bloch Institute for Solid-State Physics, Leipzig University, Leipzig 04103, Germany*

 (Received 10 August 2022; revised 27 September 2022; accepted 11 October 2022; published 23 November 2022)

Single-crystal growth, magnetic properties, and magnetocaloric effect of the $S = 3/2$ kagome ferromagnet $\text{Li}_9\text{Cr}_3(\text{P}_2\text{O}_7)_3(\text{PO}_4)_2$ (trigonal, space group: $P\bar{3}c1$) are reported. Magnetization data suggest dominant ferromagnetic intraplane coupling with a weak anisotropy and the onset of ferromagnetic ordering at $T_C \simeq 2.6$ K. Microscopic analysis reveals a very small ratio of interlayer to intralayer ferromagnetic couplings ($J_\perp/J \simeq 0.02$). Electron spin-resonance data suggest the presence of short-range correlations above T_C and confirms the quasi-two-dimensional character of the spin system. A large magnetocaloric effect characterized by isothermal entropy change of $-\Delta S_m \simeq 31$ J kg⁻¹ K⁻¹ and adiabatic temperature change of $-\Delta T_{\text{ad}} \simeq 9$ K upon a field sweep of 7 T is observed around T_C . This leads to a large relative cooling power of RCP $\simeq 284$ J kg⁻¹. The large magnetocaloric effect, together with negligible hysteresis render $\text{Li}_9\text{Cr}_3(\text{P}_2\text{O}_7)_3(\text{PO}_4)_2$ a promising material for magnetic refrigeration at low temperatures. The magnetocrystalline anisotropy constant $K \simeq -7.42 \times 10^4$ erg cm⁻³ implies that the compound is an easy-plane-type ferromagnet with the hard axis normal to the ab plane, consistent with the magnetization data.

DOI: [10.1103/PhysRevApplied.18.054076](https://doi.org/10.1103/PhysRevApplied.18.054076)

I. INTRODUCTION

Kagome lattice hosts a plethora of interesting phenomena. Its frustrated nature renders antiferromagnetic kagome insulators a natural playground for the experimental realization of quantum spin liquid [1–3]. Whereas kagome ferromagnets are not frustrated and develop magnetic order, they are no less interesting because flat bands and Dirac fermions expected in this setting have far-reaching implications for transport properties. Recent work on ferromagnetic kagome metals exposed anomalous Hall and Nernst effects, as well as chiral edge states, in several intermetallic compounds, such as Fe_3Sn_2 [4], $\text{Co}_3\text{Sn}_2\text{S}_2$ [5], LiMn_6Sn_6 [6], and $\text{UCo}_{0.8}\text{Ru}_{0.2}\text{Al}$ [7]. Concurrently, insulating kagome ferromagnets are actively studied in the context of magnon Hall effect and other exotic properties associated with Dirac magnons [8–10].

Ferromagnets are further interesting as materials with the large magnetocaloric effect (MCE) that can be instrumental in cooling via adiabatic demagnetization for reaching temperatures in the sub-Kelvin range [11–13]. This magnetic refrigeration technique is often considered as the most energy-efficient, cost-effective (as ³He and ⁴He are expensive), and environment-friendly replacement for the conventional refrigeration based on gas compression and expansion technique. For this purpose, materials with large magnetic moment, low magnetic anisotropy, low magnetic hysteresis, and extremely low transition temperature are desirable [14,15]. The nature of the magnetic transition and the specific form of the magnetic structure are also deciding factors for the performance of a MCE material. Ferromagnetic insulators with second-order phase transition are proposed to be excellent MCE materials, as only a small change in applied magnetic field is sufficient to yield a large entropy change and adiabatic temperature change, compared to any paramagnetic salt [12,15]. A very few ferromagnetic insulators with low transition temperature are reported to satisfy the above prerequisites and qualify for low-temperature applications [16–18].

*rnath@iisertvm.ac.in

In the following, we report the magnetic properties of $\text{Li}_9\text{Cr}_3(\text{P}_2\text{O}_7)_3(\text{PO}_4)_2$ (LCPP), which is a structural sibling of the recently reported $S = 5/2$ Heisenberg kagome antiferromagnet $\text{Li}_9\text{Fe}_3(\text{P}_2\text{O}_7)_3(\text{PO}_4)_2$ (LFPP) with a trigonal space group $P\bar{3}c1$ [19]. LFPP shows the onset of an antiferromagnetic (AFM) ordering below $T_N \simeq 1.3$ K and a characteristic $1/3$ magnetization plateau below $T^* \simeq 5$ K. The NMR spectra along with the NMR spin-lattice relaxation time reveal the presence of an exotic semiclassical nematic spin liquid regime between T_N and T^* . In contrast, LCPP is found to be a ferromagnet and it undergoes a ferromagnetic (FM) ordering at $T_C \simeq 2.5$ K. LCPP exhibits a large MCE around T_C and appears to have strong potential for cryogenic applications such as low-temperature sensors in space research, achieving sub-Kelvin temperatures for basic research, hydrogen and helium gas liquefaction, etc. [11,20].

II. METHODS

Platelet single crystals of LCPP with the lateral size of 0.5 to 1 mm are synthesized by a self-flux technique as reported in Ref. [21]. The mixture of starting materials, Li_3PO_4 , Cr_2O_3 , and $\text{NH}_4\text{H}_2\text{PO}_4$ in the molar ratio 15:1:9 is kept in an alumina crucible and heated gradually to 900°C . The cooling process involves three steps. At first, the sample is cooled down to 850°C at a rate of 50°C per hour and then to 600°C at a slow rate of 2°C per hour. Finally, the sample is allowed to cool naturally to room temperature. In order to dissolve the flux and separate the crystals, the sample is treated with 1 M solution of acetic acid for 5 days followed by the treatment with saturated NaCl solution and distilled water. The final product after the treatment yields the mixture of mm-sized single crystals and polycrystalline sample. The large-sized crystals are handpicked and the remaining part is grinded to get the polycrystalline sample.

Room-temperature single-crystal x-ray diffraction (XRD) is performed on a good-quality single crystal using the Bruker KAPPA APEX-II CCD diffractometer equipped with graphite monochromated $\text{MoK}\alpha_1$ radiation ($\lambda = 0.71073$ Å). The APEX3 software is used to collect the data that are further reduced with SAINT/XPREP followed by an empirical absorption correction using the SADABS program [22]. The phase purity of the polycrystalline sample is confirmed from powder XRD (PANalytical Xpert-Pro, $\text{CuK}\alpha$ radiation with $\lambda_{\text{av}} = 1.54182$ Å). The temperature-dependent powder XRD measurement is performed in the temperature range $15\text{ K} \leq T \leq 300\text{ K}$ with a low-temperature (Oxford Phenix) attachment to the diffractometer.

Magnetization (M) measurement is performed as a function of temperature (T) and magnetic field (H) using a superconducting quantum interference device (SQUID) (MPMS-3, Quantum Design) magnetometer. The data are collected in the temperature range $1.8\text{ K} \leq T \leq 350\text{ K}$ and

in the magnetic field range $0 \leq H \leq 7$ T. Heat capacity (C_p) as a function of T ($0.5\text{ K} \leq T \leq 300\text{ K}$) and H is measured on a small piece of sintered pellet using the relaxation technique in the physical property measurement system (PPMS, Quantum Design). Measurements below 2 K are carried out using an additional ^3He insert in the PPMS.

High-field electron spin-resonance (HF ESR) spectroscopy is used to study the single crystals of LCPP. For the measurements in a frequency range 75–330 GHz, a vector network analyzer (PNA-X from Keysight Technologies) is used and for frequencies up to 975 GHz a modular amplifier and multiplier chain (AMC from Virginia Diodes Inc.) is used for the generation of microwaves in combination with a hot-electron InSb bolometer for detection. All measurements are performed at a given fixed frequency in the field-sweep mode up to 16 T, using a superconducting magnet system from Oxford Inst. The sample is mounted onto a transmission probe head, which is then inserted in a ^4He variable temperature insert (VTI) of the magnet cryostat to enable measurements in a temperature range of 1.8–300 K.

Density-functional (DFT) band-structure calculations are performed in the FPLO code [23] with the Perdew-Burke-Ernzerhof flavor of the exchange-correlation potential [24]. Correlation effects in the Cr $3d$ shell are included on the mean-field level within DFT + U using the on-site Coulomb repulsion parameter $U_d = 2$ eV, Hund's coupling $J_d = 1$ eV, and double-counting correction in the atomic limit [25,26]. Exchange couplings J_{ij} are obtained by mapping [27] total energies of collinear magnetic configurations onto the spin Hamiltonian,

$$\mathcal{H} = \sum_{\langle ij \rangle} J_{ij} \mathbf{S}_i \mathbf{S}_j, \quad (1)$$

where the summation is over pairs, and $S = \frac{3}{2}$. Energies are converged on a k mesh with 64 points within the first Brillouin zone. Thermodynamic properties for the model defined by Eq. (1) are obtained from quantum Monte-Carlo simulations performed with the LOOP algorithm [28] of the ALPS simulation package [29]. Finite lattices with up to 752 sites and periodic boundary conditions are used.

III. RESULTS AND DISCUSSION

A. X-ray diffraction

The crystal structure of LCPP is solved from single-crystal XRD data with direct methods using SHELXT-2018/2 [30] and refined by the full matrix least squares on F^2 using SHELXL-2018/3, respectively [31]. Details of the crystal structure and the refined parameters are summarized in Table I. LCPP crystallizes in the trigonal space group $P\bar{3}c1$ (No. 165). The refined atomic positions at room temperature are listed in Table II. These

TABLE I. Crystallographic data for LCPP at room temperature, obtained from single-crystal XRD.

Empirical formula	Cr ₃ Li ₉ O ₂₉ P ₈
Formula weight (M_r)	930.22 g mol ⁻¹
Temperature	296(2) K
Crystal system	Trigonal
Space group	$P\bar{3}c1$
Lattice parameters	$a = 9.668(3) \text{ \AA}$ $\alpha = 90^\circ$ $b = 9.668(3) \text{ \AA}$ $\beta = 90^\circ$ $c = 13.610(6) \text{ \AA}$ $\gamma = 120^\circ$
Unit-cell volume	1101.7(8) \AA^3
Z	2
Density (calculated)	2.804 g cm ⁻³
Wavelength	0.71073 \AA
Radiation type	MoK α_1
Diffractometer	Bruker KAPPA APEX-II CCD
Crystal size	0.049 × 0.035 × 0.027 mm ³
2 θ range	2.993 to 25.997°
Index ranges	-11 ≤ h ≤ 11 -11 ≤ k ≤ 11 -16 ≤ l ≤ 16
$F(000)$	902
Reflections collected	6940
Independent reflections	735 [$R_{\text{int}} = 0.0454$]
Data, restraints, parameters	735/0/76
Goodness of fit on F^2	1.098
Final R indices [$I \geq 2\sigma(I)$]	$R1 = 0.0304$, $\omega R2 = 0.0892$
R indices (all data)	$R1 = 0.0351$, $\omega R2 = 0.0919$
Largest diff. peak and hole	+0.445/ -0.970 e × \AA^{-3}

structural parameters are in good agreement with the previous report [21].

The schematic view of the crystal structure of LCPP is presented in Fig. 1. It illustrates the corner sharing of CrO₆ octahedra and PO₄ tetrahedra forming equilateral triangles with a geometrically deformed but three-fold-symmetric kagome lattice. Though all of the Cr³⁺—Cr³⁺ distances in each hexagon are equal (approximately 4.949 \AA), the bond angles are different: three angles are approximately 146.3° and the remaining three angles are approximately 93.7°. The nearest-neighbor (NN) coupling between the Cr³⁺ ions in the ab plane is denoted by J , while the shortest interplane distance of approximately 6.903 \AA leads to a weak coupling (J_\perp) between the planes.

In order to confirm the phase purity and to scrutinize the presence of any structural distortions, powder XRD data are collected at various temperatures. Le Bail analysis of the XRD patterns is performed using the FullProf package [32] taking the initial structural parameters from the single-crystal data (Table I). Figures 2(a) and 2(b) present the powder XRD patterns at the highest ($T = 300$ K) and lowest ($T = 15$ K) measured temperatures, respectively, along with the Le Bail fits. All the peaks could be indexed

TABLE II. Crystal structure of LCPP refined using single-crystal XRD data. The atomic coordinates ($\times 10^4$) and the isotropic atomic displacement parameter U_{iso} ($\text{\AA}^2 \times 10^3$), which is defined as one third of the trace of the orthogonalized U_{ij} tensor.

Atomic sites	Wyckoff positions	x	y	z	U_{iso}
Cr(1)	6f	5676(1)	0	2500	6(1)
Li(1)	2b	0	0	5000	19(3)
Li(2)	12g	3369(7)	2367(7)	4374(4)	16(1)
Li(3)	4d	6667	3333	6178(7)	15(2)
O(1)	12g	3758(2)	-1053(2)	3331(1)	9(1)
O(2)	6f	2120(3)	0	2500	9(1)
O(3)	12g	792(2)	-2535(2)	3440(2)	9(1)
O(4)	12g	2299(3)	38(2)	4332(2)	11(1)
O(5)	12g	6781(2)	1893(2)	3352(2)	10(1)
O(6)	4d	6667	3333	4839(3)	23(1)
P(1)	12g	2279(1)	-894(1)	3440(1)	6(1)
P(2)	4d	6667	3333	3736(1)	5(1)

based on the space group $P\bar{3}c1$, suggesting phase purity of the polycrystalline sample. The obtained lattice parameters at room temperature are $a = b = 9.6628(3) \text{ \AA}$, $c = 13.5769(3) \text{ \AA}$, and unit-cell volume $V_{\text{cell}} \simeq 1097.85(5) \text{ \AA}^3$, which are consistent with the single-crystal data. No extra peaks or features are observed in the XRD data corroborating the absence of any structural transition or distortion down to 15 K.

The temperature variation of lattice parameters (a , c , and V_{cell}) is presented in Fig. 3. They are found to decrease monotonically upon cooling down to 15 K. $V_{\text{cell}}(T)$ is fitted by the equation [33]

$$V_{\text{cell}}(T) = \frac{\gamma U(T)}{K_0} + V_0, \quad (2)$$

where V_0 is the zero-temperature unit-cell volume, K_0 is the bulk modulus, and γ is the Grüneisen parameter. $U(T)$

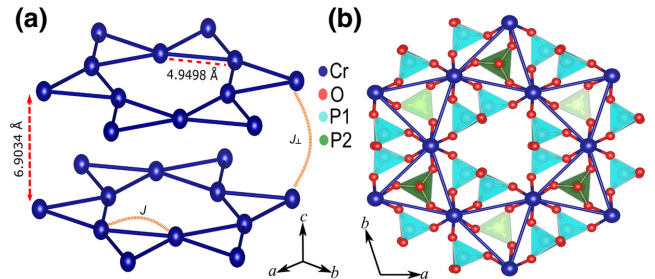


FIG. 1. (a) Corner-sharing equilateral triangles of Cr³⁺ form a kagome lattice. The intraplane (J) and interplane (J_\perp) couplings are shown. The kagome lattice layers are well separated from each other with interlayer distance of 6.9034 \AA . (b) Interactions between the magnetic Cr³⁺ ions via PO₄ tetrahedra are shown.

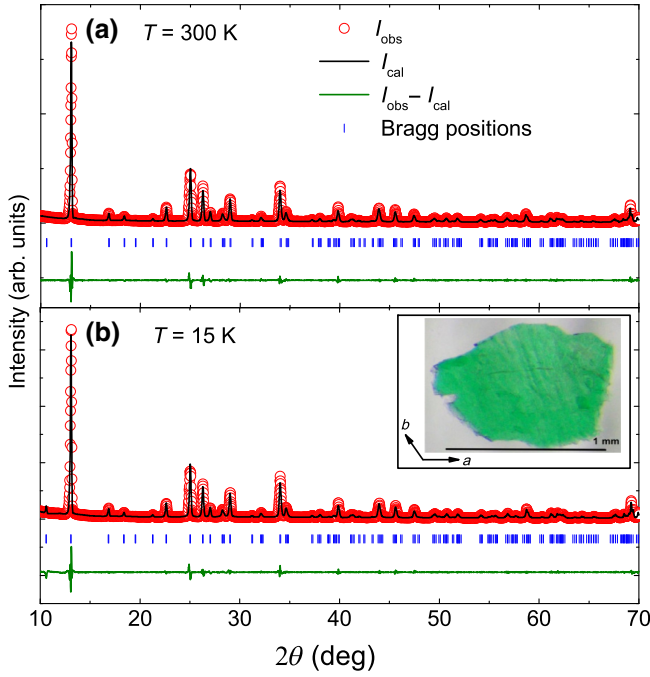


FIG. 2. Powder XRD data measured at (a) $T = 300$ K and (b) $T = 15$ K. The black solid line represents the Le Bail fit of the data. Bragg positions are indicated by vertical bars and the solid green line at the bottom denotes the difference between experimental and calculated intensities. The inset of (b) shows a representative single crystal.

is the internal energy and it can be expressed in terms of the Debye approximation as

$$U(T) = 9pk_B T \left(\frac{T}{\theta_D} \right)^3 \int_0^{\theta_D/T} \frac{x^3}{e^x - 1} dx. \quad (3)$$

Here, p is the number of atoms in the unit cell, k_B is the Boltzmann constant, and the Debye temperature is represented by θ_D . The fit (see Fig. 3) returns $\theta_D \simeq 385$ K, $\gamma/K_0 \simeq 2.06 \times 10^{-4} \text{ Pa}^{-1}$, and $V_0 \simeq 1094.2 \text{ \AA}^3$.

B. Magnetization

Magnetic susceptibility $\chi(T) [\equiv M(T)/H]$ measured in an applied field of $H = 0.5$ T perpendicular ($H \perp c$) and parallel ($H \parallel c$) to the kagome plane is displayed in Fig. 4(a). With decreasing temperature, $\chi(T)$ increases in a Curie-Weiss manner as expected in the high-temperature paramagnetic (PM) regime, followed by a rapid enhancement at low temperatures. This rapid increase suggests strong FM correlations below about 10 K. Further, the susceptibilities for $H \perp c$ and $H \parallel c$ show only a small difference even at low temperatures, which is an indication of weak magnetic anisotropy in the compound.

For a quantitative analysis, we plot the inverse susceptibility ($1/\chi$) as a function of temperature in Fig. 4(c)

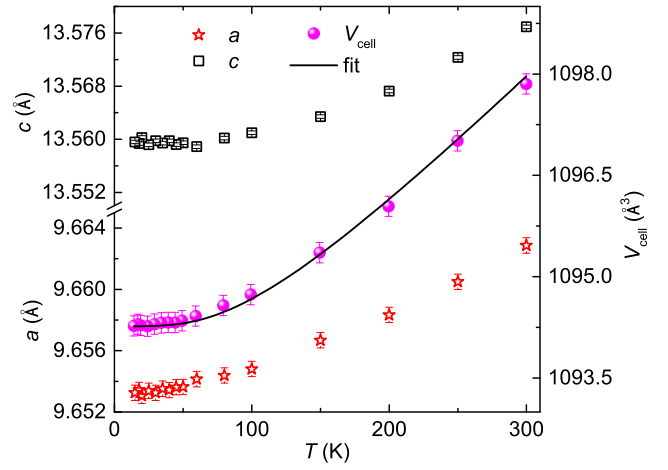


FIG. 3. Variation of lattice parameters (a , c , and V_{cell}) with temperature. The solid line denotes the fit of $V_{\text{cell}}(T)$ by Eq. (2).

for $H \perp c$. For $T \geq 50$ K, it exhibits a completely linear behavior, which is fitted by the modified Curie-Weiss (CW) law

$$\chi(T) = \chi_0 + \frac{C}{(T - \theta_{\text{CW}})}. \quad (4)$$

Here, χ_0 is the temperature-independent susceptibility, C is the Curie constant, and θ_{CW} is the CW temperature. The fit yields $\chi_0 \simeq -3.6 \times 10^{-4} \text{ cm}^3 \text{ mol}^{-1}$, $C \simeq 1.92 \text{ cm}^3 \text{ K mol}^{-1}$, and $\theta_{\text{CW}} \simeq 6$ K. From the value of C the effective moment is calculated to be $\mu_{\text{eff}} \simeq 3.92 \mu_B$ in agreement with the spin-only value of $3.87 \mu_B$ for spin $3/2$. The positive value of θ_{CW} suggests that the dominant exchange interactions between Cr^{3+} ions are FM in nature. Using the mean-field expression $J/k_B = -3|\theta_{\text{CW}}|/zS(S+1)$ with $z = 4$ neighbors on the kagome lattice, we estimate $J/k_B \simeq -1.2$ K. Moreover, the small peak in χT in low magnetic fields reveals $T_C \simeq 2.6$ K [Fig. 4(d)]. $\chi(T)$ measured in zero-field cooled and field-cooled conditions (not shown) in a small magnetic field of $H = 0.01$ T for $H \perp c$ shows no difference, suggesting negligible hysteresis.

The magnetic isotherm (M versus H) at $T = 1.8$ K saturates in low fields of $H_{\text{sat}} \perp c \simeq 0.15$ T and $H_{\text{sat}} \parallel c \simeq 0.4$ T with the saturation magnetization of $M_{\text{sat}} \sim 3.2 \mu_B/\text{Cr}^{3+}$ and $2.8 \mu_B/\text{Cr}^{3+}$ for $H \perp c$ and $H \parallel c$, respectively (not shown). The obtained M_{sat} values are close to the calculated $M_{\text{sat}} = gS\mu_B \simeq 2.952\mu_B$ and $2.937\mu_B$, taking the ESR values $g \simeq 1.968$ and 1.958 for $H \perp c$ and $H \parallel c$, respectively. No visible hysteresis is observed in any of the field directions. A slight difference in the saturation field for $H \perp c$ and $H \parallel c$ may be attributed to the anisotropic demagnetization field caused by the flat shape of the crystals [10]. The demagnetization factor is negligible when magnetic field is parallel to the crystal plates ($H \perp c$). However, when field is perpendicular to crystal plate ($H \parallel c$), the demagnetization effect is considerably amplified

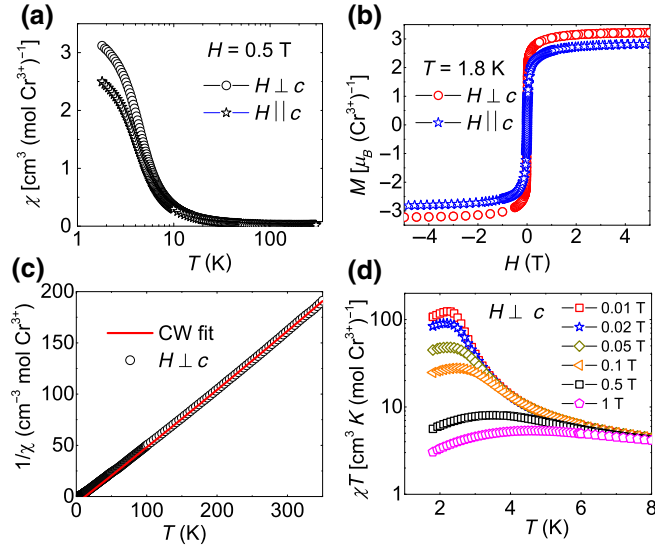


FIG. 4. (a) $\chi(T)$ measured in the field of $H = 0.5$ T applied perpendicular ($H \perp c$) and parallel ($H \parallel c$) to the c axis. (b) Magnetization at $T = 1.8$ K as a function of applied field for both $H \perp c$ and $H \parallel c$ after correcting for the demagnetization effect. (c) Inverse susceptibility ($1/\chi$) as a function of temperature for $H \perp c$ and solid line is the CW fit. (d) χT versus T in different fields for $H \perp c$ in low temperatures.

[34]. The data in Fig. 4(b) are corrected for this demagnetizing field as $H_{\text{eff}} = H_0 - 4\pi NM$ where H_{eff} and H_0 are the effective and applied magnetic fields, respectively, N is the demagnetization factor, and M is magnetic moment in emu cm^{-3} . To calculate the demagnetization factor in the case of LCPP, we approximate the shape of the sample to a rectangular strip and did the calculation following Ref. [35], which yields $N = 0.84$ for $H \parallel c$. The H_{sat} in both directions after demagnetization correction is found to be almost same (approximately 0.15 T).

C. Heat capacity

Temperature-dependent heat capacity C_p measured on the polycrystalline sample is shown in Fig. 5. The C_p data exhibit a sharp λ -type anomaly at $T_C \simeq 2.5$ K demonstrating the transition to the magnetically ordered state. Typically, in magnetic insulators, the major contributions to C_p are from magnetic (C_{mag}) and phonon (C_{ph}) parts. At high temperatures, C_{ph} dominates over C_{mag} , while at low temperatures it is reverse. One can estimate C_{mag} by subtracting C_{ph} from the total heat capacity. First, we approximate the phonon contribution by fitting the high- T data by a linear combination of one Debye and three Einstein terms as [36]

$$C_{\text{ph}}(T) = f_D C_D(\theta_D, T) + \sum_{i=1}^3 g_i C_{E_i}(\theta_{E_i}, T). \quad (5)$$

The first term in Eq. (5) is the Debye contribution to C_{ph} , which can be written as

$$C_D(\theta_D, T) = 9nR \left(\frac{T}{\theta_D} \right)^3 \int_0^{\theta_D/T} \frac{x^4 e^x}{(e^x - 1)^2} dx. \quad (6)$$

Here, R is the universal gas constant, θ_D is the characteristic Debye temperature, and n is the number of atoms in the formula unit. The second term in Eq. (5) gives the Einstein contribution to C_{ph} that has the form

$$C_E(\theta_E, T) = 3nR \left(\frac{\theta_E}{T} \right)^2 \frac{e^{\theta_E/T}}{[e^{\theta_E/T} - 1]^2}. \quad (7)$$

Here, θ_E is the characteristic Einstein temperature. The coefficients f_D , g_1 , g_2 , and g_3 represent the fraction of atoms that contribute to their respective parts. These values are taken in such a way that their sum should be equal to 1 and are conditioned to satisfy the Dulong-Petit value approximately $3nR$ at high temperatures. The high- T fit to the $C_p(T)$ data is then extrapolated down to low temperatures and subtracted from $C_p(T)$. The obtained C_{mag}/T is plotted as a function of temperature in the main panel of Fig. 5(b) and the corresponding magnetic entropy is calculated to be $S_{\text{mag}}(T) = \int_0^T [C_{\text{mag}}(T')/T'] dT' \simeq 11.6 \text{ J mol}^{-1} \text{ K}^{-1}$ at 12 K. This value corresponds to the expected magnetic entropy for spin 3/2: $S_{\text{mag}} = R \ln 4 = 11.5 \text{ J mol}^{-1} \text{ K}^{-1}$. Unlike the conventional magnets, which release the entire entropy near the transition temperature, LCPP releases only approximately 40% of the total entropy at T_C and the remaining entropy is released only above 11 K, suggesting that T_C is partially suppressed as a result of low dimensionality or magnetic frustration [26].

The inset of Fig. 5(a) presents the $C_p(T)$ data measured in different applied fields. The influence of magnetic field is clearly reflected in the data. The zero-field peak broadens and shifts toward high temperatures with increasing field, which is usual for ferromagnets. At low temperatures, $C_{\text{mag}}(T)$ in zero field could be well described using power-law ($C_{\text{mag}} \propto T^\alpha$) behavior [inset of Fig. 5(b)] with an exponent $\alpha \sim 1.5$ that corresponds to FM spin-wave excitations [37].

D. Magnetocaloric effect

MCE is an intrinsic property of magnetic materials. Magnetic cooling is achieved by first applying magnetic field to the material isothermally and then removing the field adiabatically. Therefore, MCE is generally quantified by the isothermal entropy change (ΔS_m) and adiabatic temperature change (ΔT_{ad}) with respect to the change in applied field. The ΔS_m can be calculated from either magnetization isotherms (M versus H) or heat capacity data measured in zero and nonzero magnetic fields. Figure 6(a)

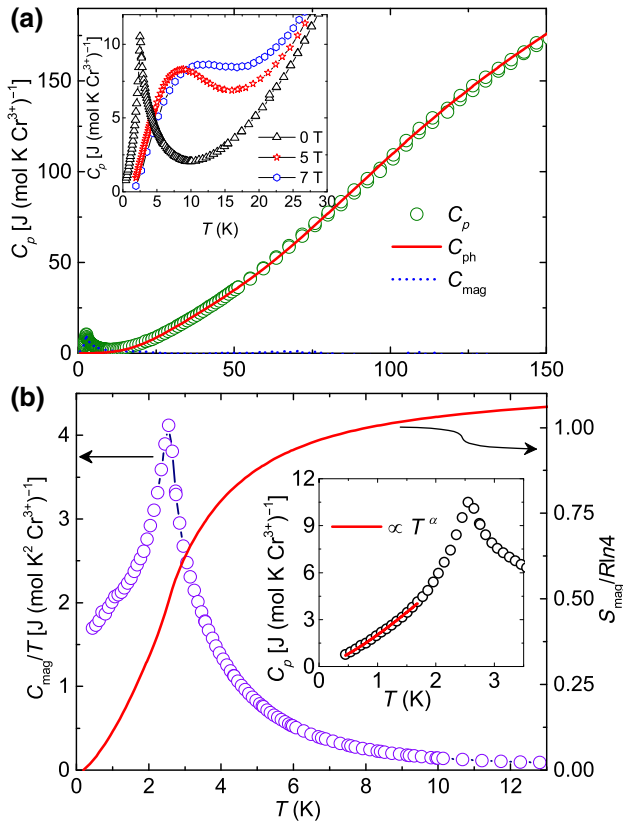


FIG. 5. (a) Heat capacity (C_p) of LCPP measured in zero applied field. The solid line represents the simulated phonon contribution [$C_{ph}(T)$] and the dotted line represents the magnetic contribution [$C_{mag}(T)$]. Inset: low-temperature C_p measured in various applied fields. (b) C_{mag}/T and $S_{mag}/R \ln 4$ in left and right y axes, respectively, are plotted as a function of temperature. Inset: $C_{mag}(T)$ versus T . Solid line is the power-law ($C_{mag} = aT^\alpha$) fit in the low- T regime.

displays the magnetic isotherms measured in close temperature steps around T_C for $H \perp c$. The first method utilizes Maxwell's thermodynamic relation, $(\partial S/\partial H)_T = (\partial M/\partial T)_H$, and ΔS_m can be estimated using the M versus H data as [38]

$$\Delta S_m(H, T) = \int_{H_i}^{H_f} \frac{dM}{dT} dH. \quad (8)$$

Figure 7(a) presents the plot of ΔS_m as a function of temperature (T) in different values of $\Delta H = H_f - H_i$. ΔS_m versus T exhibits a maximum entropy change around 4.6 K, with a highest value of $\Delta S_m \simeq -31 \text{ J kg}^{-1} \text{ K}^{-1}$ for the 7 T field change. As the magnetic anisotropy is negligibly small, no significant difference in ΔS_m is expected for $H \perp c$ and $H \parallel c$ [39].

Further, to cross-check the large value of ΔS_m , we also estimate ΔS_m from heat-capacity data measured in zero field, 5 T, and 7 T. First, we calculate the total entropy at a

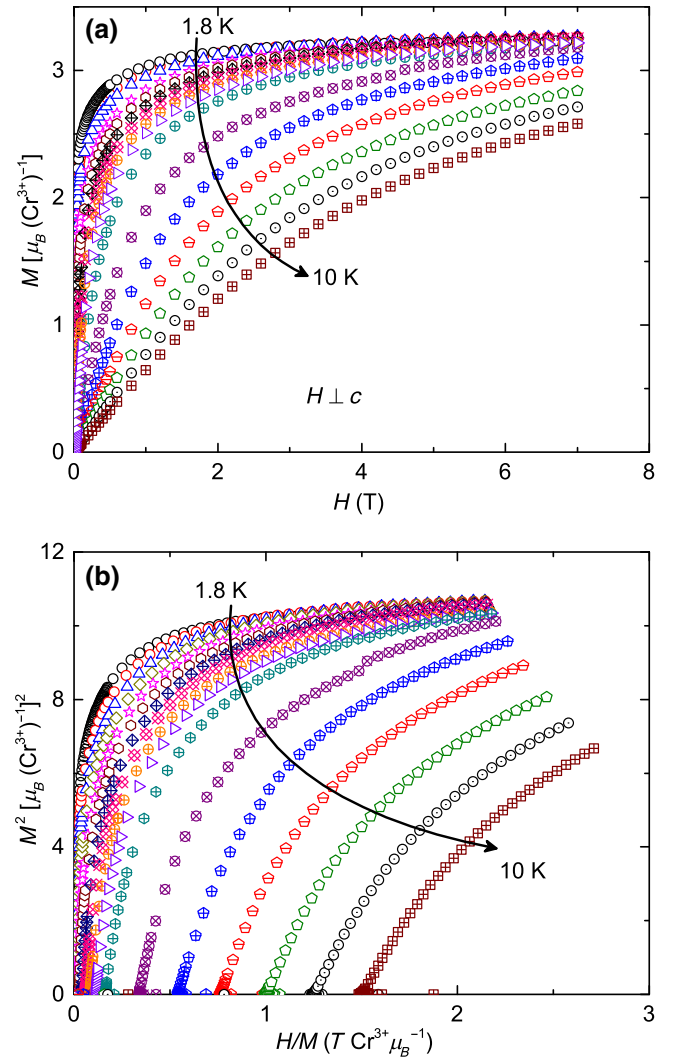


FIG. 6. (a) Isothermal magnetization (M versus H) curves for $H \perp c$ and (b) their corresponding Arrott plots [M^2 versus (H/M)] for LCPP at different temperatures around T_C .

given field as

$$S(T)_H = \int_{T_i}^{T_f} \frac{C_p(T)_H}{T} dT, \quad (9)$$

where $C_p(T)_H$ is the heat capacity at a particular field H and T_i and T_f are the initial and final temperatures, respectively. We calculate ΔS_m by taking the difference of total entropy at nonzero and zero fields as $\Delta S_m(T)_{\Delta H} = [S(T)_H - S(T)_0]_T$. Here, $S(T)_H$ and $S(T)_0$ are the total entropy in the presence of H and in zero field, respectively. Figure 7(b) presents the estimated ΔS_m as a function of temperature in 5 T and 7 T magnetic fields. The overall shape and peak position of the ΔS_m curves are identical with the curves [Fig. 7(a)] obtained from the magnetic isotherms but with a slight reduction in magnitude. This difference in magnitude at the peak position could be

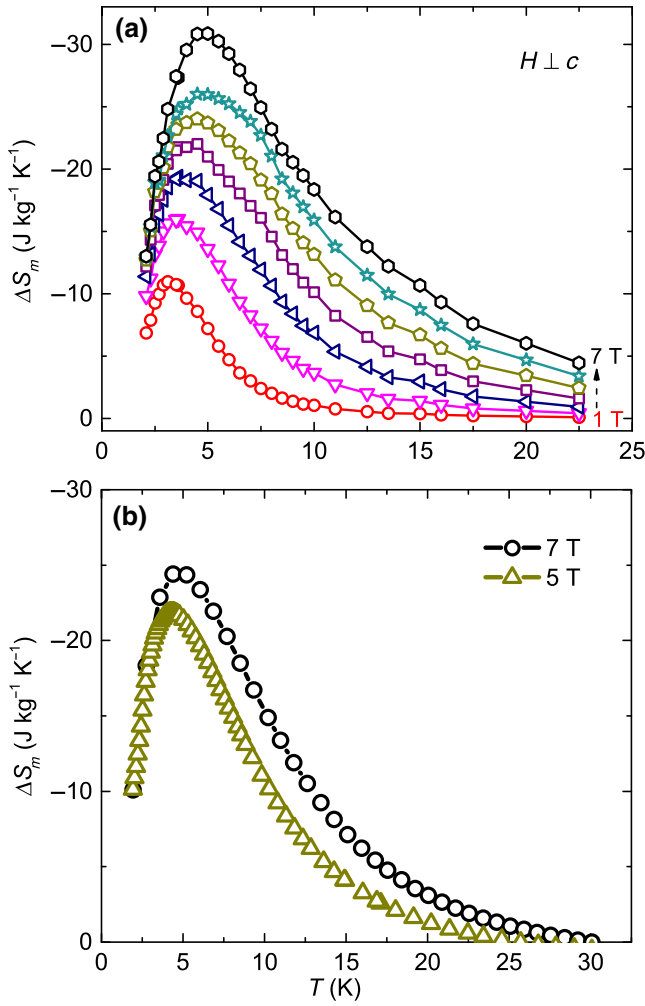


FIG. 7. (a) Isothermal entropy change (ΔS_m) versus T plotted upon sweeping the field to 0 T starting from different fields from 1 to 7 T, calculated using M versus H data of single crystals for $H \perp c$ and employing Eq. (8). (b) ΔS_m versus T plot for 5 and 7 T, calculated using $C_p(T)$ of polycrystalline sample in Eq. (9).

related to the polycrystalline sample used for heat capacity and single crystals for magnetic measurements [40].

Similarly, the adiabatic temperature change ΔT_{ad} can be estimated from either the combination of zero-field heat capacity and the magnetic entropy change obtained from magnetic isotherms or from the heat capacity alone measured in different magnetic fields. Using the heat capacity in zero field and magnetization isotherm data, the estimation of ΔT_{ad} can be done as [41]

$$\Delta T_{\text{ad}} = \int_{H_i}^{H_f} \frac{T}{C_p} \frac{dM}{dT} dH. \quad (10)$$

The dependence of ΔT_{ad} on T for different magnetic fields is shown in Fig. 8(a). The maximum value of ΔT_{ad} is

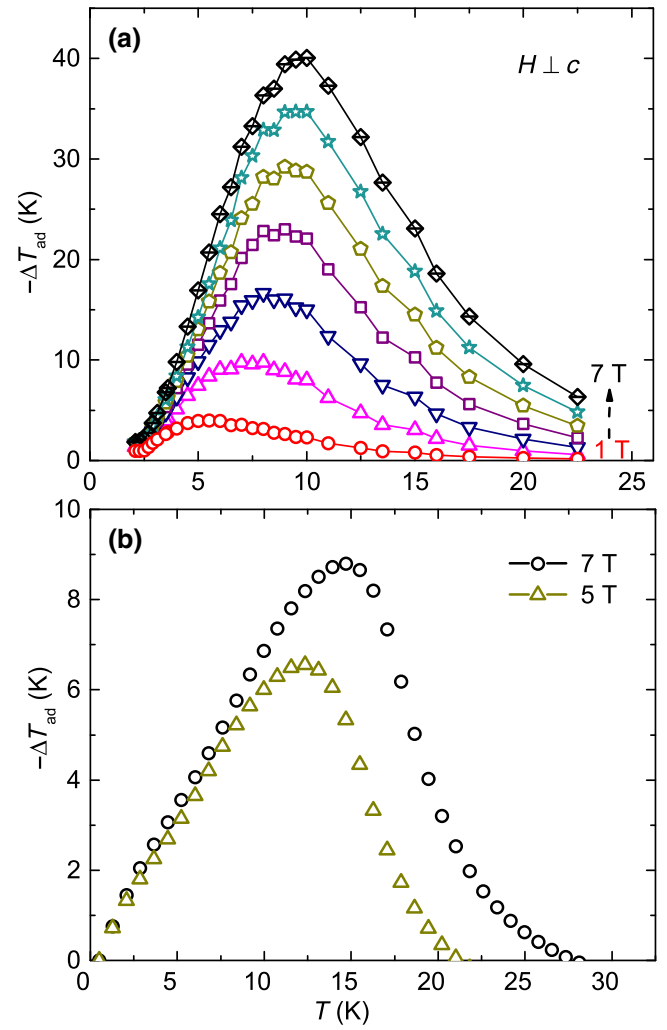


FIG. 8. (a) ΔT_{ad} versus T plotted for different field changes of $\Delta H = 1$ T to 7 T calculated using Eq. (10). (b) ΔT_{ad} versus T plotted for $\Delta H = 5$ T and 7 T calculated using Eq. (11).

obtained to be approximately 40 K for $\Delta H = 7$ T. However, as explained in Ref. [42] the above expression overestimates ΔT_{ad} since T/C_p is not constant over the range of applied fields as it is assumed. It is evident from the inset of Fig. 5(a) that C_p at low temperatures is changing drastically as we apply magnetic field and this change should be taken into account while calculating the entropy for that particular field. Therefore, we try to estimate ΔT_{ad} by taking the difference in temperatures corresponding to two different fields with constant (same) entropy as [42]

$$\Delta T_{\text{ad}}(T)_{\Delta H} = [T(S)_{H_f} - T(S)_{H_i}]. \quad (11)$$

ΔT_{ad} versus T for $\Delta H = 5$ and 7 T calculated by this method is shown in Fig. 8(b). The maximum value of ΔT_{ad} at 7 T is approximately 9 K, which is significantly smaller than the value obtained using the former method [Eq. (10)]. A similar difference has been reported earlier for ErAl_2

[42]. The latter method is considered to be more reliable. It is expected to provide accurate results as the effect of magnetic field on C_p is accounted for.

Note that the large values of ΔS_m and ΔT_{ad} are not sufficient to characterize the potential of a material for the magnetic refrigeration applications. Another parameter is the relative cooling power (RCP), which is a measure of the amount of heat transferred between the cold and hot reservoirs in a refrigeration cycle. Mathematically, it can be expressed as

$$\text{RCP} = \int_{T_{\text{cold}}}^{T_{\text{hot}}} \Delta S_m(T, H) dT, \quad (12)$$

where T_{cold} and T_{hot} correspond to temperatures of cold and hot reservoirs, respectively. The formula for RCP can be approximated as

$$|\text{RCP}|_{\text{approx}} = \Delta S_m^{\text{peak}} \times \delta T_{\text{FWHM}}, \quad (13)$$

where ΔS_m^{peak} and δT_{FWHM} are the maximum value of entropy change (or the peak value) and full width at half maximum of the ΔS_m curve, respectively. RCP as a function of H calculated using the ΔS_m data from Fig. 7(a) is plotted in Fig. 9(a). The maximum value of RCP is calculated to about 284 J kg^{-1} at 7 T.

The application of a MCE material is also decided by the nature of its magnetic phase transition. In materials with a first-order phase transition, though the peak height of the ΔS_m and ΔT_{ad} versus T curves is large but the curve width is not very broad, which limits the relevance of these materials in a cyclic operation. The second problem with the first-order transitions is the energy loss due to magnetic and thermal hysteresis [43]. Further, relatively large magnetic fields are required to perturb the first-order magnetostructural transitions and induce large MCE, which is another drawback of these materials. On the other hand, materials with second-order phase transition do not show very large peaks, but their RCP values are large due to the increased curve width and the absence of thermal hysteresis, both effects making them promising for practical applications. In order to analyze the nature of the phase transition, we construct the Arrott plot [44] in Fig. 6(b) by using the isothermal magnetization data presented in Fig. 6(a). Clearly, the slope of M^2 versus H/M curves is positive in the entire measured temperature range, well below and above T_C . According to the Banerjee criterion [45], positive slope implies the second-order phase transition. This confirms the continuous second-order nature of the PM to FM phase transition in LCPP.

Furthermore, MCE is also utilized to characterize the nature of a phase transition [41,46,47]. According to the scaling hypothesis [43], the $\Delta S_m(T)$ curves for different values of ΔH should collapse on a single universal curve when the $\Delta S_m(T)$ is normalized to its peak value ΔS_m^{peak} .

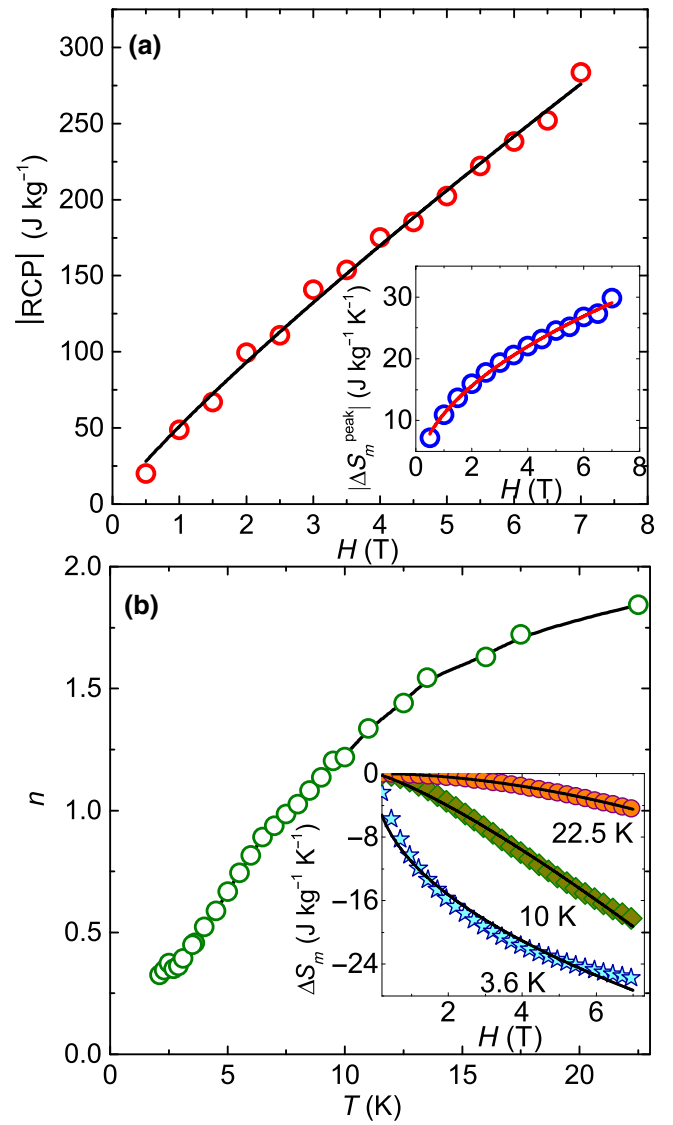


FIG. 9. (a) Relative cooling power ($\text{RCP} = \Delta S_m^{\text{peak}} \times \delta T_{\text{FWHM}}$) as a function of magnetic field and the inset shows the value of entropy change at the peak position ΔS_m^{peak} . Solid lines are the fits as described in the text. (b) The exponent n plotted as a function of temperature, which is obtained from fitting power law to ΔS_m versus H isotherms. Inset shows the ΔS_m isotherms for temperatures near and well above T_C .

However, due to the low transition temperature, the universal curve construction is implausible with the present data. Therefore, we perform only the power-law analysis of ΔS_m and RCP. In Fig. 9(a) (main panel and inset), we fit the RCP and ΔS_m^{peak} data by power laws of the form $\text{RCP} \propto H^N$ and $|\Delta S_m^{\text{peak}}| \propto H^n$, respectively. The exponents N and n , which are related to the critical exponents (β , γ , and δ), are estimated to be $N \simeq 0.7$ and $n \simeq 0.5$. In order to perceive the temperature dependence of n , we fit the field-dependent isothermal magnetic entropy change $\Delta S_m(H)$ at various temperatures across the transition using

TABLE III. Comparison of the adiabatic temperature change (ΔT_{ad}), maximum entropy change (ΔS_m^{peak}), and RCP of LCPP with some known magnets having low transition temperatures (T_C or T_N) and large MCE in a field change of $\Delta H = 5$ to 8 T. More compounds with similar behavior are listed in Refs. [40,48,49].

System	T_C/T_N (K)	$ \Delta T_{\text{ad}} $ (K)	$ \Delta S_m^{\text{peak}} $ (J kg ⁻¹ K ⁻¹)	RCP (J kg ⁻¹)	ΔH (T)	Ref.
LCPP	2.6	9	31	284	7	This work
HoMnO ₃	5	6.5	13.1	320	7	[50]
ErMn ₂ Si ₂	4.5	12.9	25.2	365	5	[18]
EuTi _{0.9} V _{0.3} O ₃	4.5	17.4	41.4	577	7	[17]
GdCrTiO ₅	0.9	15.5	36	...	7	[51]
EdDy ₂ O ₄	5	16	25	415	8	[52]
EuHo ₂ O ₄	5	12.7	30	540	8	[52]
Mn ₃₂	0.32	6.7	18.2	...	7	[53]
HoB ₂	15	12	40.1	...	5	[54]
EuTiO ₃	5.6	21	49	500	7	[48]

the power law $\Delta S_m \propto H^n$ [see inset of Fig. 9(b)] [46]. The obtained n versus T data are plotted in Fig. 9(b) and provide information concerning the nature of the transition. For instance, for a second-order magnetic transition the exponent should have the value $n \simeq 2$ in the paramagnetic region ($T \gg T_C$) and $n(T)$ typically exhibits a minimum near T_C [46]. Indeed, our $n(T)$ demonstrates the expected behavior, further confirming the second-order magnetic transition in LCPP.

In Table III, we compare the main parameters of LCPP with those of well-studied magnets having low transition temperatures and large MCE. Though the ΔS_m^{peak} value of LCPP is comparable to the values for most of the potential low-temperature magnetic refrigerant materials, the width of ΔS_m versus T curves is not very broad. Due to which LCPP has a slightly reduced value of RCP compared to others. Nevertheless, the obtained value of RCP $\simeq 284$ J kg⁻¹ is still significantly large and LCPP may have strong prerequisites for cryogenic applications in sub-Kelvin temperatures [11,20].

E. Electron spin resonance

1. Frequency dependence at $T = 1.8$ K

The ferromagnetic resonance (FMR) measurements on LCPP are performed at $T = 1.8$ K ($< T_C$) for the two orientations of the applied magnetic field, $H \parallel c$ and $H \perp c$. The frequency (ν) versus resonance field (H_{res}) dependence of the FMR signal is shown in Fig. 10 together with few selected spectra (right axis). The spectra measured at fields perpendicular to the c axis are relatively broader and more distorted when compared to the $H \parallel c$ measurements. The ν versus H_{res} data are fitted with a spin-wave model for FMR, $\nu = h^{-1}g_{\parallel}\mu_B(H_{\text{res}} - H_a)$ for $H \parallel c$ orientation and $\nu = h^{-1}g_{\perp}\mu_B[H_{\text{res}}(H_{\text{res}} + H_a)]^{1/2}$ for $H \perp c$ orientation to obtain the g factors and the anisotropy field H_a . It is found that the g factors in both orientations are somewhat different amounting to $g_{\perp} = 1.968 \pm 0.003$ and

$g_{\parallel} = 1.958 \pm 0.003$. Such a slightly anisotropic g tensor is typical for a Cr³⁺ ion ($3d^3$, $S = 3/2$, $L = 3$) in a distorted octahedral ligand coordination [55]. Further, the anisotropy field H_a is obtained as approximately 2864 Oe from the fit. Generally, H_a consists of two contributions [56]:

$$H_a = 4\pi M - 2K/M. \quad (14)$$

The first term accounts for the shape anisotropy and the second term is the intrinsic magnetocrystalline anisotropy. In Eq. (14), the first term assumes the shape anisotropy of a thin plate with $N = 1$.

Using the saturation magnetization value, $M_s = g_{\parallel}S = 2.94\mu_B/\text{Cr}^{3+}$, the magnetocrystalline anisotropy constant $K = -7.42 \times 10^4$ erg cm⁻³ is obtained. The negative sign

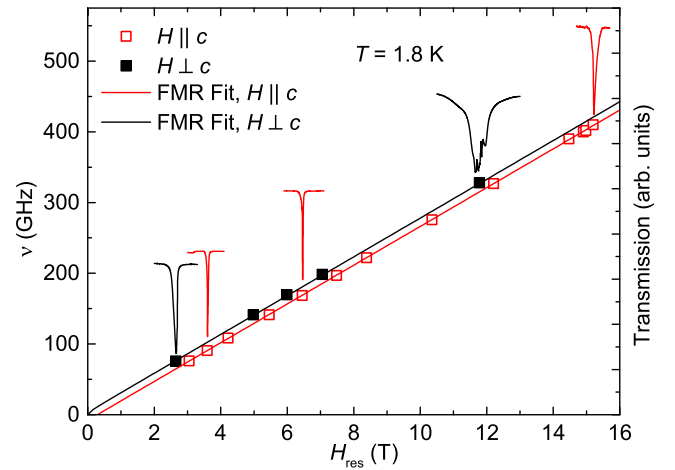


FIG. 10. Left vertical scale: frequency as a function of resonant field measured for both orientations at $T = 1.8$ K. The hollow red and solid black squares represent the measured resonance fields for orientations $H \parallel c$ and $H \perp c$, respectively. Right vertical scale: selected HF ESR spectra.

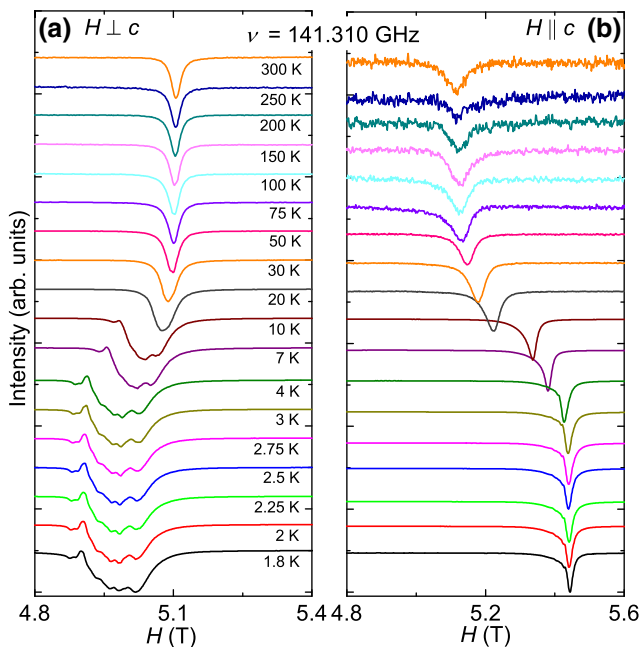


FIG. 11. Temperature dependence of the HF ESR spectra at an excitation frequency of 141.310 GHz for (a) $H \perp c$ and (b) $H \parallel c$. Line shape distortions at $T < 20$ K in the $H \perp c$ field geometry are instrumental artifacts arising due to the strong magnetization of the sample.

of K implies that LCPP is an easy-plane ferromagnet with the hard magnetic axis normal to the ab plane. We note that no other resonance excitations could be found in a frequency range up to 975 GHz (4 meV).

2. Temperature dependence

HF ESR spectra of LCPP at various temperatures are measured at a fixed excitation frequency of $\nu = 141.310$ GHz for both field directions [see Figs. 11(a) and 11(b)]. The resonance fields H_{res} are obtained from the absorption minima of each spectrum and are plotted against temperature in Fig. 12(a). Interestingly, the H_{res} versus T dependence for both orientations does not converge to a paramagnetic line immediately at $T_C = 2.8$ K. Only above 10 K, the resonance fields for $H \parallel c$ and $H \perp c$ orientations rapidly start to decrease and increase, respectively, toward the expected paramagnetic position and almost merge around 100 K at a field corresponding to the g factor, $g = 1.97$. The lineshape distortions in measurements at low temperatures for $H \perp c$ are accounted for in the enlarged error bars.

The shift of the resonance position $\delta H(T)$ from the paramagnetic one is shown in Fig. 12(b) (left y axis). $\delta H(T)$ is positive and larger when the external field is parallel to the magnetic hard axis, as compared to the smaller negative shift for the in-plane field geometry, as expected for an easy-plane ferromagnet. Such a shift cannot be ascribed

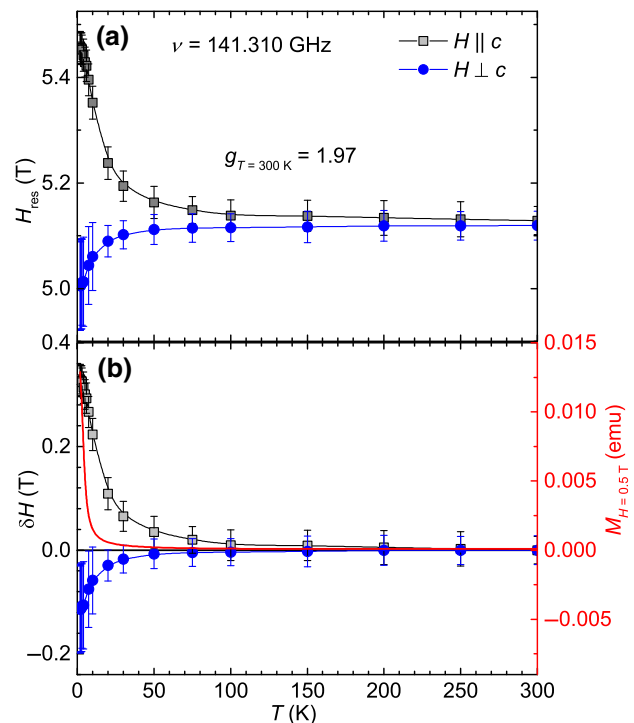


FIG. 12. Temperature dependence of (a) the resonance field H_{res} and (b) the resonance shift $\delta H = H_{\text{res}}(T) - H_{\text{res}}(300 \text{ K})$ (left y axis) and the magnetization M in an applied field of $H = 0.5$ T (right y axis), for both $H \parallel c$ and $H \perp c$.

entirely to the shape anisotropy, which should play a role also in the paramagnetic state if the sample's magnetization M is large. The $M(T)$ curve plotted in Fig. 12(b) (right y axis) for comparison decreases right above T_C more rapidly than the $\delta H(T)$ dependence. Therefore, the line shift observed for both orientations well above the Curie temperature may be indicative of short-range FM spin correlations on the fast ESR time scale, typical for low-dimensional magnets such as, e.g., the quasi-two-dimensional van der Waals compound $\text{Cr}_2\text{Ge}_2\text{Te}_6$ [57]. This is also the case for LCPP owing to its layered crystal structure.

F. Microscopic analysis

Our DFT calculations return nearest-neighbor exchange coupling $J/k_B \simeq -0.5$ K within the kagome planes. This value is somewhat dependent on the choice of the DFT+ U parameters, but the negative sign is robust and suggests the ferromagnetic nature of the kagome network in LCPP. The origin of this ferromagnetic coupling deserves some attention, as the sibling Fe^{3+} compound is clearly antiferromagnetic [19]. Superexchange theory stipulates that antiferromagnetic couplings are mediated by hoppings between half-filled orbitals, whereas ferromagnetic couplings arise from hoppings between the half-filled and empty orbitals. In LCPP with the $3d^3$ Cr^{3+} magnetic ion,

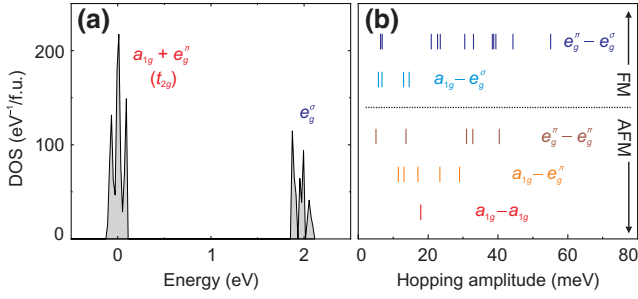


FIG. 13. (a) PBE density of states for LCPP with the Fermi level placed at zero energy. (b) Nearest-neighbor Cr–Cr hopping amplitudes within the kagome plane.

these orbitals have the t_{2g} and e_g^σ characters, respectively. Trigonal symmetry of the crystal structure further splits the t_{2g} levels into a_{1g} and e_g^π .

DFT band structure of LCPP calculated on the PBE level features narrow t_{2g} ($a_{1g} + e_g^\pi$) bands around the Fermi level and almost equally narrow e_g^σ bands centered at around 2.0 eV (Fig. 13). This band structure is metallic because neither magnetism nor correlation effects are taken into account. The small band width of 0.25 eV for the t_{2g} bands indicates that antiferromagnetic contribution to the exchange couplings should be minor. The $t_{2g} - e_g^\sigma$ hoppings are small too, but somewhat larger than the $t_{2g} - t_{2g}$ hoppings, as shown in Fig. 13(b). Therefore, ferromagnetic contribution to the exchange becomes predominant, and the overall coupling is ferromagnetic. Magnetic susceptibility of LCPP is well described by the model of nearest-neighbor ferromagnetic kagome planes with $J/k_B = -1.2$ K ($g = 1.995$). A minute interlayer coupling $J_\perp/J = 0.01$ improves the fit below 3.5 K and leads to the Curie temperature $T_C = 2.8$ K in a perfect agreement with the experimental $T_C \simeq 2.6$ K (Fig. 14). Our DFT calculations corroborate this result and reveal a weakly ferromagnetic J_\perp with $J_\perp/J \simeq 0.02$.

IV. SUMMARY

We synthesize single crystals of LCPP and confirm trigonal $P3c1$ symmetry of this compound with the lattice constants $a = b = 9.668(3)$ Å and $c = 13.610(6)$ Å at room temperature. Green-colored LCPP is a rare example of an insulating kagome ferromagnet. Ferromagnetic order below $T_C \simeq 2.6$ K is driven by the in-plane FM coupling $J/k_B \simeq -1.2$ K supplied with a minute interplane coupling $J_\perp/J = 0.02$, which is also FM in nature. The incomplete release of the magnetic entropy at T_C and the increased width of the ESR line above T_C both suggest quasi-2D magnetic behavior caused by the strong spatial anisotropy of FM couplings. The overall magnetic behavior of LCPP has striking resemblance with that of other insulating kagome ferromagnets, such as α -MgCu₃(OD)₆Cl₂ and Cu[1,3-bdc] [10,58]. Magnetization

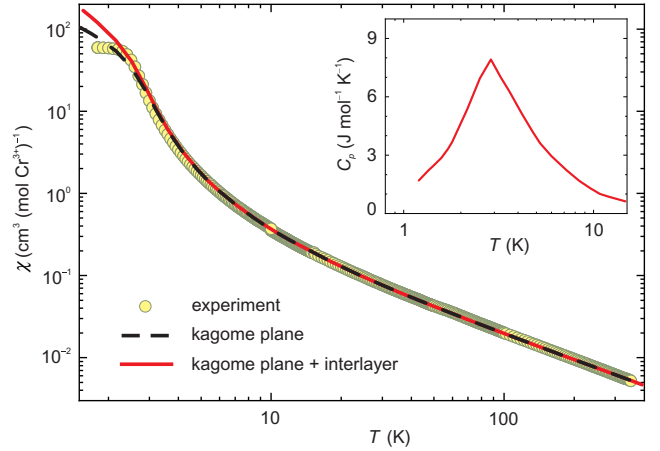


FIG. 14. Magnetic susceptibility of LCPP measured in the applied field of 0.01 T upon field cooling and its fit using the model of ferromagnetic kagome planes (dashed line) and coupled ferromagnetic kagome planes ($J_\perp/J = 0.01$, solid line). The inset shows calculated heat capacity for the coupled kagome planes, with $T_C \simeq 2.8$ K.

and ESR measurements on single crystals indicate a weak easy-plane anisotropy. The critical scaling of magnetization suggests a non-mean-field-type second-order nature of the phase transition at T_C . The low T_C combined with the large values of ΔS_m , ΔT_{ad} , and RCP render LCPP a promising magnetocaloric material for low-temperature applications.

ACKNOWLEDGMENTS

A.M., S.K., V.S., and R.N. would like to acknowledge SERB, India for financial support bearing sanction Grant No. CRG/2019/000960. The ESR work in Dresden was supported by the Deutsche Forschungsgemeinschaft (DFG) through grants No. KA 1694/12-1, AL 1771/8-1, and within the Collaborative Research Center SFB 1143 “Correlated Magnetism- From Frustration to Topology” (project-id 247310070), and the Dresden-Würzburg Cluster of Excellence (EXC 2147) “ct.qmat - Complexity and Topology in Quantum Matter” (project-id 39085490).

- [1] P. Mendels and F. Bert, Quantum kagome frustrated antiferromagnets: One route to quantum spin liquids, *C. R. Phys.* **17**, 455 (2016).
- [2] T.-H. Han, J. S. Helton, S. Chu, D. G. Nocera, J. A. Rodriguez-Rivera, C. Broholm, and Y. S. Lee, Fractionalized excitations in the spin-liquid state of a kagome-lattice antiferromagnet, *Nature* **492**, 406 (2012).
- [3] J. Carrasquilla, Z. Hao, and R. G. Melko, A two-dimensional spin liquid in quantum kagome ice, *Nat. Commun.* **6**, 7421 (2015).
- [4] L. Ye, M. Kang, J. Liu, F. von Cube, C. R. Wicker, T. Suzuki, C. Jozwiak, A. Bostwick, E. Rotenberg, D. C. Bell,

- L. Fu, R. Comin, and J. G. Checkelsky, Massive Dirac fermions in a ferromagnetic kagome metal, *Nature* **555**, 638 (2018).
- [5] S. Howard, L. Jiao, Z. Wang, N. Morali, R. Batabyal, P. Kumar-Nag, N. Avraham, H. Beidenkopf, P. Vir, E. Liu, C. Shekhar, C. Felser, T. Hughes, and V. Madhavan, Evidence for one-dimensional chiral edge states in a magnetic Weyl semimetal $\text{Co}_3\text{Sn}_2\text{S}_2$, *Nat. Commun.* **12**, 4269 (2021).
- [6] D. Chen, C. Le, C. Fu, H. Lin, W. Schnelle, Y. Sun, and C. Felser, Large anomalous Hall effect in the kagome ferromagnet LiMn_6Sn_6 , *Phys. Rev. B* **103**, 144410 (2021).
- [7] T. Asaba, V. Ivanov, S. M. Thomas, S. Y. Savrasov, J. D. Thompson, E. D. Bauer, and F. Ronning, Colossal anomalous Nernst effect in a correlated noncentrosymmetric kagome ferromagnet, *Sci. Adv.* **7**, eabf1467 (2021).
- [8] A. Mook, J. Henk, and I. Mertig, Magnon Hall effect and topology in kagome lattices: A theoretical investigation, *Phys. Rev. B* **89**, 134409 (2014).
- [9] R. Chisnell, J. S. Helton, D. E. Freedman, D. K. Singh, R. I. Bewley, D. G. Nocera, and Y. S. Lee, Topological Magnon Bands in a Kagome Lattice Ferromagnet, *Phys. Rev. Lett.* **115**, 147201 (2015).
- [10] R. Chisnell, J. S. Helton, D. E. Freedman, D. K. Singh, F. Demmel, C. Stock, D. G. Nocera, and Y. S. Lee, Magnetic transitions in the topological magnon insulator $\text{Cu}(1,3\text{-bdc})$, *Phys. Rev. B* **93**, 214403 (2016).
- [11] K. A. Gschneidner Jr, V. K. Pecharsky, and A. O. Tsokol, Recent developments in magnetocaloric materials, *Rep. Prog. Phys.* **68**, 1479 (2005).
- [12] V. K. Pecharsky and K. A. Gschneidner Jr, Magnetocaloric effect and magnetic refrigeration, *J. Magn. Magn. Mater.* **200**, 44 (1999).
- [13] A. Kitanovski, Energy applications of magnetocaloric materials, *Adv. Energy Mater.* **10**, 1903741 (2020).
- [14] V. Franco, J. Blázquez, J. Ipus, J. Law, L. Moreno-Ramírez, and A. Conde, Magnetocaloric effect: From materials research to refrigeration devices, *Prog. Mater. Sci.* **93**, 112 (2018).
- [15] M.-H. Phan and S.-C. Yu, Review of the magnetocaloric effect in manganite materials, *J. Magn. Magn. Mater.* **308**, 325 (2007).
- [16] J. K. Murthy, K. D. Chandrasekhar, S. Mahana, D. Topwal, and A. Venimadhav, Giant magnetocaloric effect in $\text{Gd}_2\text{NiMnO}_6$ and $\text{Gd}_2\text{CoMnO}_6$ ferromagnetic insulators, *J. Phys. D: Appl. Phys.* **48**, 355001 (2015).
- [17] S. Roy, M. Das, and P. Mandal, Large low-field magnetic refrigeration in ferromagnetic insulator $\text{EuTi}_{0.9}\text{V}_{0.1}\text{O}_3$, *Phys. Rev. Mater.* **2**, 064412 (2018).
- [18] L. Li, K. Nishimura, W. D. Hutchison, Z. Qian, D. Huo, and T. NamiKi, Giant reversible magnetocaloric effect in ErMn_2Si_2 compound with a second order magnetic phase transition, *Appl. Phys. Lett.* **100**, 152403 (2012).
- [19] E. Kermarrec, R. Kumar, G. Bernard, R. Hénaff, P. Mendels, F. Bert, P. L. Paulose, B. K. Hazra, and B. Koteswararao, Classical Spin Liquid State in the $S = \frac{5}{2}$ Heisenberg Kagome Antiferromagnet $\text{Li}_9\text{Fe}_3(\text{P}_2\text{O}_7)_3(\text{PO}_4)_2$, *Phys. Rev. Lett.* **127**, 157202 (2021).
- [20] M.-J. Martínez-Pérez, O. Montero, M. Evangelisti, F. Luis, J. Sesé, S. Cardona-Serra, and E. Coronado, Fragmenting gadolinium: Mononuclear polyoxometalate-based magnetic coolers for ultra-low temperatures, *Adv. Mater.* **24**, 4301 (2012).
- [21] S. Poisson, F. d'Yvoire, N. Guyen-Huy-Dung, E. Bretey, and P. Berthet, Crystal structure and cation transport properties of the layered monodiphosphates: $\text{Li}_9\text{M}_3(\text{P}_2\text{O}_7)_3(\text{PO}_4)_2$ ($M = \text{Al, Ga, Cr, Fe}$), *J. Solid State Chem.* **138**, 32 (1998).
- [22] G. M. Sheldrick, *Siemens Area Correction Absorption Correction Program* (University of Göttingen, Göttingen, Germany, 1994).
- [23] K. Koepernik and H. Eschrig, Full-potential nonorthogonal local-orbital minimum-basis band-structure scheme, *Phys. Rev. B* **59**, 1743 (1999).
- [24] J. P. Perdew, K. Burke, and M. Ernzerhof, Generalized Gradient Approximation Made Simple, *Phys. Rev. Lett.* **77**, 3865 (1996).
- [25] O. Janson, G. Nénert, M. Isobe, Y. Skourski, Y. Ueda, H. Rosner, and A. A. Tsirlin, Magnetic pyroxenes $\text{LiCrGe}_2\text{O}_6$ and $\text{LiCrSi}_2\text{O}_6$: Dimensionality crossover in a nonfrustrated $S = \frac{3}{2}$ Heisenberg model, *Phys. Rev. B* **90**, 214424 (2014).
- [26] K. Somesh, Y. Furukawa, G. Simutis, F. Bert, M. Prinz-Zwick, N. Büttgen, A. Zorko, A. A. Tsirlin, P. Mendels, and R. Nath, Universal fluctuating regime in triangular chromate antiferromagnets, *Phys. Rev. B* **104**, 104422 (2021).
- [27] H. J. Xiang, E. J. Kan, S.-H. Wei, M.-H. Whangbo, and X. G. Gong, Predicting the spin-lattice order of frustrated systems from first principles, *Phys. Rev. B* **84**, 224429 (2011).
- [28] S. Todo and K. Kato, Cluster Algorithms for General- S Quantum Spin Systems, *Phys. Rev. Lett.* **87**, 047203 (2001).
- [29] A. F. Albuquerque *et al.* The ALPS project release 1.3: Open-source software for strongly correlated systems, *J. Magn. Magn. Mater.* **310**, 1187 (2007).
- [30] G. M. Sheldrick, Shelxt-integrated space-group and crystal-structure determination, *Acta Crystallogr. A: Found. Adv.* **71**, 3 (2015).
- [31] G. M. Sheldrick, *Shelxl-2018/3 Software Package* (University of Göttingen, Germany, 2018).
- [32] J. Rodríguez-Carvajal, Recent advances in magnetic structure determination by neutron powder diffraction, *Physica B* **192**, 55 (1993).
- [33] S. J. Sebastian, S. S. Islam, A. Jain, S. M. Yusuf, M. Uhlarz, and R. Nath, Collinear order in the spin- $\frac{5}{2}$ triangular-lattice antiferromagnet $\text{Na}_3\text{Fe}(\text{PO}_4)_2$, *Phys. Rev. B* **105**, 104425 (2022).
- [34] E. Morosan, L. Li, N. P. Ong, and R. J. Cava, Anisotropic properties of the layered superconductor $\text{Cu}_{0.07}\text{TiSe}_2$, *Phys. Rev. B* **75**, 104505 (2007).
- [35] R. Prozorov and V. G. Kogan, Effective Demagnetizing Factors of Diamagnetic Samples of Various Shapes, *Phys. Rev. Appl.* **10**, 014030 (2018).
- [36] S. J. Sebastian, K. Somesh, M. Nandi, N. Ahmed, P. Bag, M. Baenitz, B. Koo, J. Sichelschmidt, A. A. Tsirlin, Y. Furukawa, and R. Nath, Quasi-one-dimensional magnetism in the spin- $\frac{1}{2}$ antiferromagnet $\text{BaNa}_2\text{Cu}(\text{VO}_4)_2$, *Phys. Rev. B* **103**, 064413 (2021).

- [37] E. Gopal, *Specific Heats at low Temperatures* (Springer, Boston, MA, 2012).
- [38] A. M. Tishin and Y. I. Spichkin, *The Magnetocaloric Effect and its Applications* (CRC Press, London, 2016), 1st ed., p. 476.
- [39] M. Balli, S. Jandl, P. Fournier, and M. M. Gospodinov, Anisotropy-enhanced giant reversible rotating magnetocaloric effect in HoMn_2O_5 single crystals, *Appl. Phys. Lett.* **104**, 232402 (2014).
- [40] Y. Zhu, P. Zhou, T. Li, J. Xia, S. Wu, Y. Fu, K. Sun, Q. Zhao, Z. Li, Z. Tang, Y. Xiao, Z. Chen, and H.-F. Li, Enhanced magnetocaloric effect and magnetic phase diagrams of single-crystal GdCrO_3 , *Phys. Rev. B* **102**, 144425 (2020).
- [41] S. S. Islam, V. Singh, K. Somesh, P. K. Mukharjee, A. Jain, S. M. Yusuf, and R. Nath, Unconventional superparamagnetic behavior in the modified cubic spinel compound $\text{LiNi}_{0.5}\text{Mn}_{1.5}\text{O}_4$, *Phys. Rev. B* **102**, 134433 (2020).
- [42] V. K. Pecharsky and K. A. Gschneidner, Magnetocaloric effect from indirect measurements: Magnetization and heat capacity, *J. Appl. Phys.* **86**, 565 (1999).
- [43] V. Franco, J. S. Blázquez, B. Ingale, and A. Conde, The magnetocaloric effect and magnetic refrigeration near room temperature: Materials and models, *Annu. Rev. Mater. Res.* **42**, 305 (2012).
- [44] R. Nath, V. O. Garlea, A. I. Goldman, and D. C. Johnston, Synthesis, structure, and properties of tetragonal $\text{Sr}_2M_3\text{As}_2\text{O}_2$ ($M_3 = \text{Mn}_3, \text{Mn}_2\text{Cu}, \text{and MnZn}_2$) compounds containing alternating CuO_2 -type and FeAs -type layers, *Phys. Rev. B* **81**, 224513 (2010).
- [45] B. Banerjee, On a generalised approach to first and second order magnetic transitions, *Phys. Lett.* **12**, 16 (1964).
- [46] V. Singh, P. Bag, R. Rawat, and R. Nath, Critical behavior and magnetocaloric effect across the magnetic transition in $\text{Mn}_{1+x}\text{Fe}_{4-x}\text{Si}_3$, *Sci. Rep.* **10**, 6981 (2020).
- [47] V. Singh and R. Nath, Negative thermal expansion and itinerant ferromagnetism in $\text{Mn}_{1.4}\text{Fe}_{3.6}\text{Si}_3$, *J. Appl. Phys.* **130**, 033902 (2021).
- [48] A. Midya, P. Mandal, K. Rubi, R. Chen, J.-S. Wang, R. Mahendiran, G. Lorusso, and M. Evangelisti, Large adiabatic temperature and magnetic entropy changes in EuTiO_3 , *Phys. Rev. B* **93**, 094422 (2016).
- [49] Y.-Z. Zheng, G.-J. Zhou, Z. Zheng, and R. E. P. Wippeny, Molecule-based magnetic coolers, *Chem. Soc. Rev.* **43**, 1462 (2014).
- [50] A. Midya, P. Mandal, S. Das, S. Banerjee, L. S. S. Chandra, V. Ganesan, and S. R. Barman, Magnetocaloric effect in HoMnO_3 crystal, *Appl. Phys. Lett.* **96**, 142514 (2010).
- [51] M. Das, S. Roy, N. Khan, and P. Mandal, Giant magnetocaloric effect in an exchange-frustrated GdCrTiO_5 antiferromagnet, *Phys. Rev. B* **98**, 104420 (2018).
- [52] A. Midya, N. Khan, D. Bhoi, and P. Mandal, Giant magnetocaloric effect in magnetically frustrated EuHo_2O_4 and EuDy_2O_4 compounds, *Appl. Phys. Lett.* **101**, 132415 (2012).
- [53] M. Evangelisti, A. Candini, M. Affronte, E. Pasca, L. J. de Jongh, R. T. W. Scott, and E. K. Brechin, Magnetocaloric effect in spin-degenerated molecular nanomagnets, *Phys. Rev. B* **79**, 104414 (2009).
- [54] P. B. D. Castro, K. Terashima, T. D. Yamamoto, Z. Hou, S. Iwasaki, R. Matsumoto, S. Adachi, Y. Saito, P. Song, H. Takeya, and Y. Takano, Machine-learning-guided discovery of the gigantic magnetocaloric effect in HoB_2 near the hydrogen liquefaction temperature, *NPG Asia Mater.* **12**, 35 (2020).
- [55] A. Abragam and B. Bleaney, *Electron Paramagnetic Resonance of Transition Ions* (Oxford University Press, Oxford, 2012).
- [56] M. Farle, Ferromagnetic resonance of ultrathin metallic layers, *Rep. Prog. Phys.* **61**, 755 (1998).
- [57] J. Zeisner, A. Alfonsov, S. Selzer, S. Aswartham, M. P. Ghimire, M. Richter, J. van den Brink, B. Büchner, and V. Kataev, Magnetic anisotropy and spin-polarized two-dimensional electron gas in the van der Waals ferromagnet $\text{Cr}_2\text{Ge}_2\text{Te}_6$, *Phys. Rev. B* **99**, 165109 (2019).
- [58] D. Boldrin, B. Fåk, M. Enderle, S. Bieri, J. Ollivier, S. Rols, P. Manuel, and A. S. Wills, Haydeelite: A spin- $\frac{1}{2}$ kagome ferromagnet, *Phys. Rev. B* **91**, 220408 (2015).